Journal of
Materials Chemistry A

ROYAL SOCIETY
OF CHEMISTRY

PAPER

View Article Online
View Journal | View Issue

Check for updates

Cite this: *J. Mater. Chem. A*, 2026, **14**, 21080

Mechanistic mapping of alkali-ion storage in micro-spherical closed-pore hard carbon: electrochemical, *ex situ*, and DFT approaches

Nagmani, *[abc] Deepak Kumar Gorai,[b] Priyanka Pal,[c] Sanchita Manna,[a]
Raju Kumar Gupta[bc] and Sreeraj Puravankara *[a]

Received 29th December 2025
Accepted 9th April 2026

DOI: 10.1039/d5ta10571d

rsc.li/materials-a

Investigating porous closed-pore hard carbon (HC) anodes is crucial for advancing alkali-ion batteries. In this comprehensive study, electrochemical evaluations revealed that HC anodes demonstrated a notable reversible capacity of 422 mAh g^{-1} at 0.1C for SIBs, with 57% of this capacity originating from low-potential plateau regions, thus establishing a benchmark for undoped HCs. Similar performance was observed for LIBs (444 mAh g^{-1}, ∼25% more than graphite) and PIBs (235 mAh g^{-1}), accompanied by excellent cycling stability. To elucidate the ion storage mechanisms, we combined electrochemical analyses, differential capacity plots, and the galvanostatic intermittent titration technique (GITT) with *ex situ* characterization (Raman, EPR, and XPS), *operando* XRD and density functional theory (DFT) simulations. The sloping capacity region arises from defect-assisted adsorption (AC) and intercalation (IC) facilitated by edge defects and expanded graphitic layers. In contrast, the plateau region originates from insertion followed by pore filling, leading to pseudo-metallic cluster formation. *Operando* XRD provides direct structural evidence of ion-dependent reversible interlayer expansion. EPR confirmed metallic clusters at 0 V for Na and Li, supporting the pore-filling (FC) mechanism, while DFT calculations revealed that alkali-ion binding energetics depend strongly on interlayer spacing and micropore diameter, favouring Na-ion and K-ion storage in expanded graphitic layers and smaller micropores. Mechanistic analysis established the capacity contribution order as: LIBs: FC < AC < IC; SIBs: IC < AC < FC; and PIBs: FC < IC < AC. These insights bridge experimental and theoretical understanding, providing a framework for designing next-generation alkali-ion battery anodes.

Introduction

Sodium-ion batteries (SIBs) and potassium-ion batteries (KIBs) are considered promising alternatives to lithium-ion batteries (LIBs) for large-scale and low-cost energy storage applications due to the high natural abundance and low cost of Na and K, their redox chemistry comparable to Li, and the ever-increasing global demand and limited lithium resources. Graphite is the commercial go-to LIB anode, but its inability to intercalate Na ions effectively and the sluggish K-ion kinetics limit its application in SIBs and KIBs.[1–3] Consequently, non-graphitizable carbons, commonly referred to as hard carbons (HCs), have emerged as leading anode candidates for both SIBs and KIBs because of their tunable microstructure, large interlayer spacing, hierarchical porosity, and favourable mechanical/electronic properties.[4–9] The electrochemical performance of HCs is critically governed by their morphology and pore microstructure. High-surface-area, nano-sized HCs offer improved rate performance but suffer from low initial coulombic efficiency (ICE) due to sodium loss in the first cycle from extensive solid–electrolyte interphase (SEI) formation.[10,11] Conversely, low-surface-area, micro-sized HCs (<200 m^2 g^{-1}) generally deliver higher ICE and stable plateau capacity, characteristic of battery-type anodes, but are limited by sluggish ion kinetics.[12,13] The poor rate performance can be tuned by controlling the surface morphology, surface area, porosity, and surface defects in the carbon matrix and by optimization of electrolyte salts, solvents, and additives.[14–17] HCs are structurally complex, consisting of randomly oriented, curved graphene sheets, turbostratically stacked nanodomains, abundant defects, and micro/mesopores. This heterogeneity provides diverse alkali-ion storage sites, including defect/edge adsorption, interlayer intercalation, and pore filling.[18,19] The storage mechanism of alkali ions in HCs is still ambiguous due to their diverse structures, which is highly dependent on the precursor for HCs and heat treatment temperatures. Several mechanistic

---

[a] School of Energy Science & Engineering, Indian Institute of Technology Kharagpur, Kharagpur-721302, West Bengal, India. E-mail: nagmani@iitkgp.ac.in; sreeraj@iitkgp.ac.in

[b] Department of Sustainable Energy Engineering, Indian Institute of Technology Kanpur, Kanpur-208016, Uttar Pradesh, India

[c] Department of Chemical Engineering, Indian Institute of Technology Kanpur, Kanpur-208016, Uttar Pradesh, India

models have been proposed to understand the structural features and electrochemical storage of lithium, sodium, and potassium in HCs.[20–24] Typically, the voltage profiles exhibit two distinct regions: (i) a sloping region above ~0.1 V, generally ascribed to surface/defect adsorption and, in some models, partial intercalation; and (ii) a low-voltage plateau, widely debated to arise from either interlayer insertion or pore filling, depending on the alkali-ion type and local structure. Li-ion intercalation into graphitic interlayers (~3.35 Å) is energetically favourable. In contrast, Na-ion intercalation is thermodynamically unfavourable unless the interlayer spacing exceeds ~3.8 Å.[25,26] Further, the pore filling of Na ions at low potential, often leading to quasi-metallic cluster formation in closed pores, has been identified as a dominant contributor to the plateau capacity.[27,28] Despite significant advances, the fundamental understanding of alkali-ion storage mechanisms in HCs remains incomplete, especially for closed-pore architectures where pore accessibility, ion binding energetics, and diffusion pathways are intricately coupled. Advanced *operando* and *ex situ* techniques, such as XRD, solid-state NMR, SAXS/WAXS, Raman, XPS, and EPR, combined with density functional theory (DFT) calculations, have provided valuable insights into ion distribution and evolution within different carbon motifs.[29–33] However, systematic studies comparing Li-, Na-, and K-storage dynamics within a controlled HC morphology are still scarce.

This work comprehensively investigates the electrochemical behaviour and ion storage dynamics of Li ions, Na ions, and K ions in sucrose-derived micro-spherical hard carbons (MSHCs) with a closed-pore architecture. This morphology provides an optimal balance between surface-controlled and diffusion-controlled processes, enabling high reversible capacity, stable cycling, and improved rate performance. A combination of electrochemical techniques, such as galvanostatic charge–discharge, cyclic voltammetry (CV), electrochemical impedance spectroscopy (EIS), differential capacity (dQ/dV) analysis, and the galvanostatic intermittent titration technique (GITT), with *ex situ* characterization (Raman spectroscopy, X-ray photoelectron spectroscopy, electron paramagnetic resonance) and *operando* XRD was employed to deconvolute the contributions from defect adsorption, interlayer intercalation, and pore filling across the three alkali-ion systems. Furthermore, density functional theory (DFT) calculations were performed to provide atomic-scale insights into the binding energetics and preferred storage sites in pseudographitic and microporous domains, allowing direct correlation between experimental observations and theoretical predictions of Li-, Na-, and K-ion storage mechanisms.

Results and discussion

The hierarchical, porous, closed-pore hard carbon with a spherical morphology was prepared using a previously reported method.[34] This method successfully induced more defects, diverse pore-size distributions, and a high degree of compaction, enabling the synthesis of homogeneous electrodes. Detailed characterization revealed that the MSHCs exhibit a combination of disordered, oxygen-rich defects (including ultramicropores, micropores, and mesopores) and randomly dispersed ordered graphitic structures. The MSHCs were investigated as anodes in CR-2032 coin cells for Li, Na, and K-ion batteries. The galvanostatic discharge–charge profile (Fig. 1a) displays the first and second cycles of Li, Na, and K. The MSHC delivers high reversible capacities of 444 mAh g^{-1} for Li, 422 mAh g^{-1} for Na, and 235 mAh g^{-1} for K. Excellent capacity retention of 85%, 83% and 79% for Li, Na, and K was observed after 100 cycles (Fig. 1b). Fig. 1c displays the excellent rate performance of the MSHC at different current rates. The specific discharge capacities for Li/Na/K were 444/422/235 mAh g^{-1}, 330/352/174 mAh g^{-1}, 275/290/144 mAh g^{-1}, 225/251/101 mAh g^{-1}, 165/185/83 mAh g^{-1}, 98/140/52 mAh g^{-1}, and 42/92/25 mAh g^{-1} at current rates of 0.1C, 0.2C, 0.5C, 1C, 2C, 5C, and 10C, respectively. Notably, although Na$^+$ delivers slightly lower capacity than Li$^+$ at 0.1C, it surpasses both Li$^+$ and K$^+$ at higher current rates, highlighting its superior rate capability. The comparatively improved electrochemical behaviour of Na$^+$ relative to Li$^+$ and K$^+$ can be partly attributed to differences in electrolyte solvation and the resulting interfacial ion-transport characteristics and storage mechanism. Na$^+$ undergoes a combination of surface adsorption and pore-filling processes, allowing for efficient ion diffusion and reduced transport resistance within the carbon matrix,[35] especially in the case of HC with a spherical morphology. In contrast, Li$^+$ experiences slower intercalation due to higher desolvation energy. K$^+$, despite having low desolvation energy, suffers from limited accessibility to internal pores because of its larger ionic radius. These differences are evident from the reversible capacity loss percentage observed after 40 rate-test cycles, which is 2.8% for Na$^+$, compared to 13.7% and 15.2% for Li$^+$ and K$^+$, respectively. Furthermore, as shown in Fig. 1d, Na$^+$ exhibits excellent long-term cycling stability, retaining 84% of its capacity after 500 cycles at 1C, which is superior to the retention values for Li$^+$ (81%) and K$^+$ (67%) ions.

Correlation with the charge-storage mechanism

The first discharge cycle exhibits distinct electrochemical features for Li, Na, and K cells, reflecting their different ion

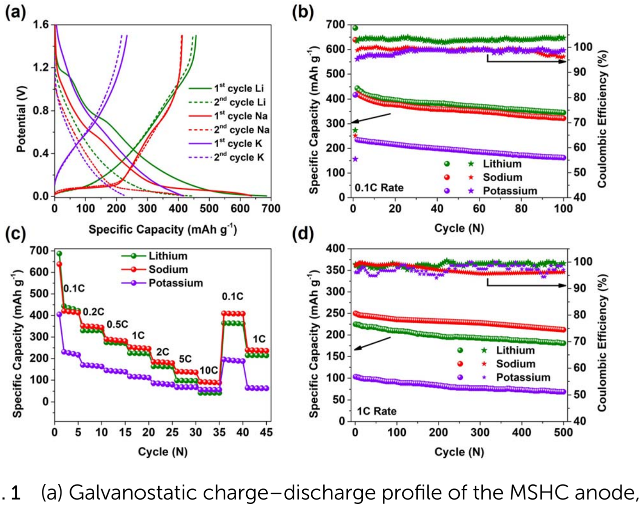

Fig. 1 (a) Galvanostatic charge–discharge profile of the MSHC anode, (b) cycling stability at a 0.1C rate (100 cycles), (c) C-rate performance, and (d) prolonged cycling at a 1C rate for 500 cycles.

storage mechanisms and interfacial reactions (Fig. 1a and S3). In the Li cell (green curve), two plateau-like regions appear at approximately 1.1 V and 0.7–0.8 V, whereas the Na cell (red curve) shows only a single plateau near 0.6–0.7 V, and the K cell displays a largely sloping profile with only a minimal plateau around 0.7 V. The additional high-voltage plateau (~1.1 V) observed exclusively for Li arises from its stronger interaction with surface functional groups and the electrolyte, leading to earlier onset of electrolyte decomposition and SEI formation. Because of its smaller ionic radius (0.76 Å) and higher charge density, Li^+ is highly polarizing and can readily reduce surface oxygenated species (C═O and –OH) and electrolyte components even at higher potentials, producing inorganic (Li_2CO_3 and LiF) and organic ($ROCO_2Li$) compounds that constitute the initial SEI layer. These irreversible reactions consume Li^+ and electrons, and once a stable passivating SEI is formed, the 1.1 V plateau disappears in subsequent cycles.[36,37] In contrast, Na^+ and K^+ ions, being larger and less polarizing, interact more weakly with the carbon surface and electrolyte molecules. Consequently, their surface and electrolyte reduction processes occur at lower potentials (~0.6–0.7 V). The smaller driving force for SEI nucleation and slower diffusion of K^+ further suppress distinct plateau formation, resulting in predominantly capacitive-type storage behaviour.

Moreover, the reversible discharge profile of the MSHC shows a sloping profile at higher potential (above 0.1 V) and a plateau profile below 0.1 V, suggesting a different charge-storage mechanism. In Fig. 2a, we correlated the contribution of sloping capacity (SC) and plateau capacity (PC) with cycling at a 0.1C rate. In the Li cells, the sloping profile (66%) is more significant than the plateau profile (44%), showing almost 87% SC retention for 100 cycles. In addition, SC is more pronounced (>96%) for the K cells, with a SC retention of 78.5%. Meanwhile, the plateau profile dominates (57%) in Na-cells, without fading significantly over cycling, suggesting excellent selectivity as a battery-type anode material for sodium storage. The capacity contributions (%) of SC and PC at different current rates of 0.1C, 0.5C, 1C, 5C and 10C are shown in Fig. 2b. At a lower C rate, PC contribution is more and gradually fades to 5C for Li and Na cells. At the same time, SC contributes significantly at higher C rates, especially for K cells. The plateau profiles disappear at higher C-rates, primarily due to the slower alkali-ion diffusion. The bigger ionic size of K^+ experienced difficulties in diffusion into the interlayer and nanopores, resulting in a pseudo-plateau (<4%) at 0.1C and no plateau beyond the 0.5C rate. Interestingly, the limited low-voltage plateau behaviour in K-cells also contributes to improved safety. Because the potassiation potential of the MSHC anode lies above the K-metal plating potential, the likelihood of metallic potassium deposition and dendrite formation is significantly reduced, making the K-cell a safer storage system.[28]

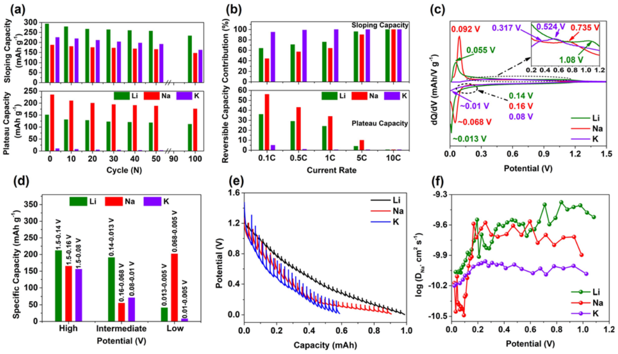

Fig. 2 Sloping and plateau capacity dependence on (a) the cycle number at a 0.1C rate and (b) C-rates for Li-, Na-, and K-cells. (c) differential capacity *versus* potential plot, (d) reversible capacity contribution as a function of potential, (e) normalized GITT profile, and (f) diffusion coefficient value obtained from the GITT.

The kinetics of alkali ion insertion in different potential regions were quantified using the differential capacity *versus* potential profile, as shown in Fig. 2c. We have separated the capacities into three distinct potential regions based on the observed lithiation/sodiation/potassiation peaks, as shown in Fig. 2d. The potential from 1.5 V to 0.14/0.16/0.08 V for Li/Na/K is mainly associated with the surface adsorption-based capacity (AC) and initialization of insertion between the graphene interlayers (IC).[20]

The peaks located at 0.013/0.068/0.01 V for Li/Na/K signify the formation of possible GICs (LiC_6, NaC_8, and KC_8) and the start of the pore-filling storage mechanism (PFC) leading to pseudo-metallic clusters. Similarly, as shown in the figure, delithiation/sodiation/potassiation peaks are observed. The MSHC electrode exhibits distinct capacities (AC) in the higher potential (HP) region. Li^+ exhibits higher adsorption capacity in the high-voltage region due to its smaller ionic radius and greater charge density, enabling stronger polarization and binding with defect or edge sites of hard carbon. In contrast, the larger, less polarizing Na^+ and K^+ ions face steric hindrance, resulting in a reduced AC. In the intermediate potential (IP) region, MSHC/Li shows a superior capacity of up to 191 mAh g^{-1}, revealing the formation of a stable intercalated compound. Further, IC is found to be more for potassium (74 mAh g^{-1}) than sodium (55 mAh g^{-1}), which could be due to the thermodynamically more stable KC_x compound than NaC_x.[27,28] The GITT profile of the MSHC in all three cells is shown in Fig. 2e. In the HP region, the gradual decrease in DC (most clearly visible for the Li system) is attributed to progressive occupation of surface adsorption sites. As these sites fill, repulsive interactions between adsorbed ions increase, reducing ion mobility and leading to the observed decline in DC. This behaviour is characteristic of surface adsorption-dominated storage. In contrast, the IP region marks the onset of intercalation into graphitic-like microdomains, where ions must overcome stronger host–guest interactions and higher activation barriers. This results in a more pronounced reduction in DC compared to the HP region. For Na specifically, the DC drops much more sharply than for Li or K. This steep decline reflects the inherently unstable nature of Na–GICs, sharply suppressing Na^+ diffusion kinetics near ~0.1 V. Moreover, unlike Li and K, the Na system maintains lower DC values even in the LP region, indicating that pore filling in Na is strongly influenced by the instability of the preceding intercalation process, which reduces the mobility of Na^+ even as it transitions into confined nanopores. Entering the

LP region, once the limited intercalation domains become saturated, ions begin to populate nanopores and closed microvoids. This pore-filling process is assisted by the preceding intercalation step, leading to an extended plateau for MSHC/Na and a subsequent increase in DC, consistent with more facile ion movement within confined pore spaces. The pore-filling capacity (PFC) of ~202 mAh g^{-1} for Na supports this mechanism.

Finally, the MSHC/K system exhibits consistently low DC throughout all three regions, reflecting sluggish kinetics primarily due to the large bare ionic radius of K^+. Although K^+ has a small Stokes radius and favourable desolvation energy, its large size restricts access to internal pores and severely limits intercalation, resulting in lower reversible capacity and inferior cycling stability compared to Li and Na systems.

Fig. 3a and S4a–c show the CV curve of MSHC in Li-, Na-, and K-cells at different scan rates from 0.1 to 1.0 mV s^{-1}. The nature of the curve signifies the combination of the faradaic (diffusion-controlled) and non-faradaic (capacitive-controlled) processes. Further, for a qualitative evaluation of the specific contribution, scan rate (ν) *versus* peak current (i), based on the power-law relationship: $i = a\nu^b$, where i is the measured current and ν is the scan rate, was plotted. The constants a and b are obtained from the intercept and slope of this plot, respectively. A b value close to 0.5 indicates that the charge storage process is predominantly diffusion-controlled, while a b value near 1 suggests a capacitive-dominated mechanism.[38] Fig. 3b shows the qualitatively quantified b-values at different potentials, indicating the pseudocapacitive nature of the MSHC electrode. The b value increases from Na to Li to K, suggesting a more diffusion-controlled mechanism for Na and a more capacitive-controlled process for K. In addition, this analysis supports the storage mechanism revealed in the above discussion. Here, it is observed that the diffusive contribution is more dominant at lower potentials and gradually decreases, while the capacitive contribution increases as a function of potential. Further, we quantified the contribution ratio of diffusive and capacitive controlled processes using Trasatti's and Dunn's methods, as shown in Fig. 3c and S4d–f.[1] The capacitive contribution increases from 58%/56%/78% to 91%/78%/97% for the Li/Na/K system, respectively. Interestingly, a significant diffusion contribution in the Na system persists even at higher scan rates, indicating a distinct sodium storage mechanism compared to Li and K. This observation suggests that the pore-filling mechanism plays a more critical role in Na-ion storage in hard carbon. In contrast, the higher capacitive contributions observed in the Li and K systems are advantageous for achieving superior rate performance.[39]

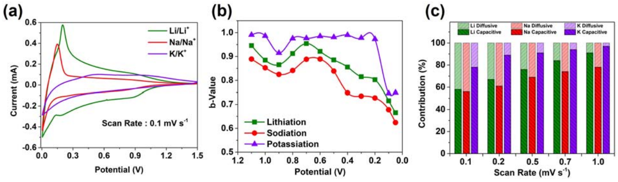

Fig. 3 (a) Combined cyclic voltammogram curve at a scan rate of 0.1 mV s^{-1}, (b) b-values quantified as a function of potential during lithiation, sodiation, and potassiation, and (c) normalized capacity contribution ratio of capacitive and diffusion-controlled processes of 20DEG-HC in all three systems.

Ex situ EPR was used to further support the creation of metallic clusters. Hard carbon shows no EPR signal, as there are no delocalized electrons or free radicals (Fig. S5a). The EPR spectra consist of two components: a broad symmetric line (Lorentzian) and a narrow asymmetric peak (Dysonian). While discharging to 5 mV, the intensity of the broad Lorentzian (symmetric) EPR signal increases as the electron density changes at the Fermi level of the carbon (Fig. 4a). Upon discharging to 0 V, a narrow asymmetric EPR signal emerges, representing electrochemical metal cluster formation for LIBs and SIBs, similar to previous results.[23,40,41] The Dysonian asymmetry parameter A/B for LIBs and SIBs is 1.13 and 1.28, respectively (the absolute ratio of the maximum to the minimum signal), which is consistent with metallic cluster formation rather than metal plating. However, PIBs show only a weakly asymmetric signal ($A/B = 1.05$), which is nearly symmetric and suggests minimal or no metallic cluster formation. The g values for LIBs, SIBs, and KIBs are 2.0024, 2.0026, and 2.003, respectively.

XPS was employed to further confirm the presence of ionic and metallic states of potassium and sodium when the MSHC discharged to 0 mV. Fig. 4b shows that the Na 1s spectra have one small peak at 1071.9 eV, attributed to the oxide form of sodium (Na_xO). Moreover, a broad peak at 1070.5 eV belongs to the metallic state of sodium,[40] supports the sodium-pore filling mechanism and leads to pseudo-metallic clustering. Besides, the K 2p spectral (Fig. 4c) peaks at 291.1 eV and 293.9 eV could be ascribed to K-$2p_{1/2}$ and K-$2p_{3/2}$, with a peak separation of 2.8 eV, confirming the ionic state of potassium.[42,43] Further insight into interfacial chemistry is obtained from the *ex situ* deconvoluted C 1s, O 1s, and F 1s spectra (Fig. S6), which reveal the formation of comparable SEI components in both Na- and K-ion systems, arising from electrolyte decomposition. Although the overall chemical nature of the surface species is

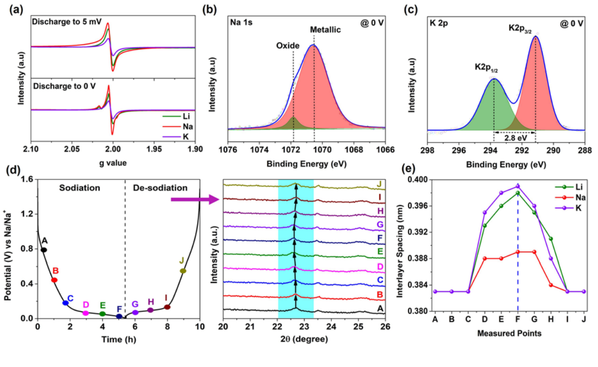

Fig. 4 *Ex situ* characterization of the discharged electrode: (a) EPR spectra, (b) XPS deconvoluted Na-1s spectra, and (c) K-2p spectra. (d) *Operando* XRD patterns of the MSHC electrode in Na-cells recorded during the first discharge–charge cycle at a current density of 50 mA g^{-1} at room temperature. (e) Corresponding evolution of the interlayer spacing as a function of electrochemical state.

qualitatively similar, the relatively stronger accumulation of Na-derived components suggests more extensive confinement-assisted storage within closed nanopores. In contrast, the comparatively lower surface enrichment of K-containing species supports a storage process dominated by surface adsorption and limited penetration into porous domains. Overall, combining *ex situ* EPR, XPS and electrochemical analysis indicates that the true pore-filling mechanism is more pronounced in SIBs and pseudo-pore-filling for PIBs till 0 V. In PIBs, this "pseudo pore-filling" behaviour arises because K ions interact mainly with pore entrances or defect-rich surface regions rather than fully penetrating the nanopores, which naturally leads to a nearly symmetric EPR response ($A/B = 1.05$) and the absence of metallic K cluster formation. An *ex situ* Raman study of the discharged cells to a potential of 5 mV is presented in Fig. S5b for insight into the lithiation/sodiation/potassiation of the MSHC. The broadening and slight downshift of the G-band are observed, most noticeably for Li, suggesting the formation of staged GICs.[32,44] However, the weakening/disappearance of the D-band is still puzzling. It could arise from the formation of the SEI layer[44,45] or intercalation into the carbon structure.[46] The low resolution prevents making definitive statements regarding the precise D-band and G-band shift.

To provide direct structural validation of alkali-ion insertion, we have performed *operando* XRD measurements. The *operando* XRD patterns for Li-, Na-, and K-cells recorded during the first discharge–charge cycle (1.5 V–5 mV) are presented in Fig. 4d and S7. In all three systems, the (002) diffraction peak at ~22.7° remains essentially unchanged in the initial sloping region (A–C), indicating that charge storage in this potential range is primarily surface-controlled and does not involve significant interlayer expansion. Upon further discharge, a clear shift of the (002) peak towards lower diffraction angles is observed for the Li system (D–F), corresponding to an increase in interlayer spacing from ~0.383 nm to ~0.396 nm. This reversible lattice expansion provides direct evidence of Li-ion intercalation into turbostratic graphitic domains. A comparatively larger apparent expansion (~0.398 nm) is observed during potassiation, which can be attributed to structural strain and partial insertion near graphitic domains due to the larger ionic radius of the K ion. In contrast, the Na system shows only a minor shift of the (002) peak (~22.6°), corresponding to negligible interlayer expansion. This indicates that Na-ion insertion into turbostratic layers is limited and that the dominant low-potential storage mechanism arises from intercalation-assisted pore filling within closed nanopores rather than classical intercalation. During the subsequent charging process (G–J), the (002) peak position in all three systems returns to its initial value within experimental uncertainty, confirming the reversible structural evolution of the carbon framework. Furthermore, the variation of interlayer spacing with the electrochemical state (Fig. 4e) clearly shows that structural expansion follows the trend Li $\approx$ K $\gg$ Na, consistent with the different storage pathways identified from electrochemical kinetics, *ex situ* spectroscopy, and DFT calculations. These *operando* results therefore provide direct structural validation of the mechanistic mapping proposed in this work, namely intercalation-assisted storage in Li, pore-filling-dominated storage in Na, and strain-assisted surface/interlayer storage in K. Further studies are currently in progress to gain deeper insight into these features.

In summary, SC is associated with defect-assisted adsorption (AC) due to defects/edges of the graphitic sheets and the partial contribution of defect-assisted insertion (IC) into graphitic layers. In contrast, PC corresponds to the insertion followed by pore-filling (PC) of nanopores, leading to pseudo-metallic clusters. Moreover, we proposed the order of capacity contribution as (i) PC < AC < IC for MSHC/Li, (ii) IC < AC < PC for MSHC/Na, and (iii) PC < IC < AC for MSHC/K. It suggests that the hierarchical pore structure and defects benefit sodium storage, whereas larger interlayer spacing with defects is vital for LIBs and PIBs.

To gain deeper insight into the alkali-ion (Li, Na, and K) storage mechanism in hard carbon, *ab initio* DFT calculations were carried out. Two representative microstructural motifs of hard carbon, planar graphitic layers and micropores, were modelled using an AB-stacked graphite bilayer and a single-walled carbon nanotube (CNT), respectively (Fig. 5a and b). These correspond to the pseudo-graphitic and microporous nanodomains of hard carbon. The effects of interlayer distance (L) in the planar graphitic layers and pore diameter (D) in the micropores on the alkali-ion binding energy were systematically investigated. It should be noted that the DFT models used in this work represent simplified structural motifs of the disordered hard carbon framework. While such models do not fully capture the structural heterogeneity of real hard carbon, including variations in defect density, pore geometry, and stacking disorder, they provide well-defined adsorption environments that allow a direct comparison of ion–host interactions. Therefore, the calculated binding energies should be

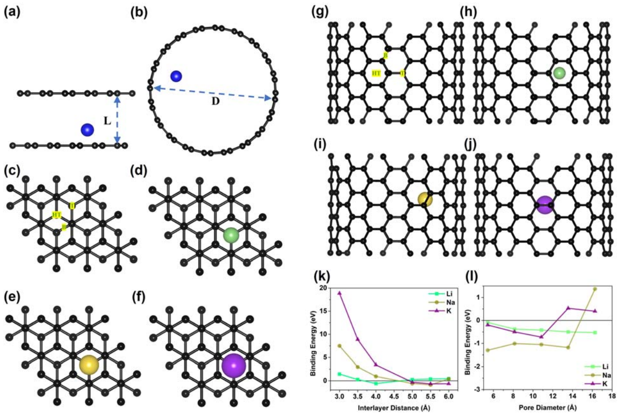

Fig. 5 Schematic representation of the intercalation of the alkali ion into the (a) planar graphitic layer and (b) micropore (single-walled CNT). The carbon (C) and alkali elements are colored in black and blue, respectively. (c) Inequivalent metal adsorption sites on a planar graphitic layer. The most stable adsorption configurations of (d) Li, (e) Na, and (f) K ions on a planar graphitic layer. (g) Inequivalent metal adsorption sites on a micropore model. The most stable adsorption configurations of (h) Li, (i) Na, and (j) K ions on a micropore model. (k) The binding energies of alkali ions in the planar graphitic layers as a function of interlayer distance (L). (l) The binding energies of alkali ions in the micropores as a function of diameter (D).

interpreted as representative qualitative trends rather than absolute quantitative values for the practical material. Fig. 5c and g illustrate the inequivalent alkali-ion adsorption sites on a planar graphitic layer and within a micropore model, respectively, which serve as the representative structural domains of hard carbon in our DFT analysis. All three alkali ions preferentially bind to the hollow-top (HT) site for the planar graphitic layers, as shown in Fig. 5d–f.

In contrast, in the micropore, the most stable adsorption configurations of Li, Na, and K are on the hollow-top (HT) site, bridge (B) site, and bridge (B) site, respectively (Fig. 5h–j). Fig. S8–S13 display the configurations of different alkali ions inserted into the planar graphitic layers at various interlayer distances and into the micropores of different diameters. The calculated binding energies for alkali ions in planar graphitic layers as a function of interlayer distance are shown in Fig. 5k. Na and K exhibit negative binding energies in the ranges $\approx$4.6–5.8 Å and $\approx$4.8–6.0 Å, respectively, while Li shows negative binding energies only between $\approx$3.5 and 4.7 Å.[47] This indicates that Na and K storage is energetically favoured at larger interlayer spacings than Li, consistent with their larger ionic radii and solvation structures.[48] At interlayer distances above $\approx$5.6 Å, the binding energy for K becomes lower (more negative) than for Li and Na, suggesting enhanced thermodynamic stability for K storage in widely spaced graphitic layers, similar to the trend observed in Olsson *et al.*, where K storage benefits from expanded lattice spacing.[49] Fig. 5l presents the binding energy dependence on micropore diameter. Na exhibits the lowest binding energy for pore diameters up to $\approx$15 Å. In comparison, K shows a pronounced binding minimum around $\approx$12.8 Å before increasing at larger diameters, suggesting that Na and K preferentially occupy smaller micropores than Li. Importantly, the binding energies for micropores are consistently more negative than planar layers, underscoring the stronger affinity of alkali ions for pore sites. This trend parallels the findings of Olsson *et al.*, who showed that cylindrical pores offer more favourable adsorption energetics than planar domains. These results highlight that, in hard carbon containing both pseudo-graphitic layers and micropores, the "pore-filling" process will dominate alkali-ion storage, particularly in the low voltage plateau region.[50] Nevertheless, the present calculations reveal general tendencies rather than precise optimum pore sizes; further studies are required to pinpoint the critical pore dimensions for maximum storage efficiency. The suitably spaced graphitic layers and appropriately sized micropores offer a synergistic pathway for high-capacity alkali-ion storage in hard carbon.

EIS was used to understand the insertion kinetics of MSHC anodes at the insertion state after the first reversible cycle. The Nyquist graphs (Fig. S14a–c) in LIBs, NIBs, and PIBs showed one depressed semicircle in the high-to-mid frequency region and the Warburg diffusion line in a low-frequency range. The shape of the semicircle deviates from an ideal single-arc response, indicating the presence of more than one relaxation process, even though these processes are not fully separated visually. The Nyquist plots were fitted with the equivalent circuit to gain insight into the reaction kinetics. According to the fitted circuit, the resistance R_1 at a high frequency is due to the electrolyte solution, and R_2 and R_3 in a medium frequency range are attributed to the SEI resistance and charge transfer resistance, respectively. Constant phase elements (CPEs), which represent non-ideal capacitive behavior, are connected in parallel with R_2 and R_3 in the equivalent circuit; W_1 is the Warburg constant arising due to phase transformation and ion diffusion in the MSHC anode.[51] The radius of the high-frequency depressed semicircles increases from Li to Na to K, suggesting that the kinetics deteriorate as the ionic diameter increases. As shown in Fig. S14d, the charge transfer resistance (R_2) of Li is lower than that of Na, reflecting fast electron/ion charge-transfer kinetics.[21] The huge R_3 for K indicates that the ion kinetics becomes worse with a larger K-ion radius, as revealed by GITT analysis.

Conclusions

In summary, we demonstrate that sucrose-derived microspherical hard carbon is a single, versatile anode material for high-performance alkali-ion batteries. The synthesized MSHC possesses a defect-rich carbon framework with expanded interlayer spacing and a well-developed hierarchical pore structure, comprising ultramicropores, supermicropores, and mesopores, collectively facilitating efficient ion transport and diffusion. Among the three systems studied, MSHC/Na delivers a reversible capacity of 422 mAh g^{-1} at 0.1C with a dominant low-potential plateau ($\sim$57%), representing one of the best performances reported for undoped hard carbon. In addition, the MSHC anode achieves reversible capacities of 444 and 235 mAh g^{-1} for Li- and K-ion cells, respectively, while maintaining excellent cycling stability and rate capability. By correlating the sloping and plateau regions in the charge–discharge profiles with electrochemical kinetic analyses and *ex situ* characterization, we reveal that the sloping region is associated with defect-assisted adsorption due to defects/edges of the graphitic sheets and defect-assisted insertion into graphitic layers. In contrast, the plateau region corresponds to the insertion followed by nanopore filling, leading to pseudo-metallic clusters. *Operando* XRD further provides direct structural validation of ion-dependent reversible interlayer expansion, enabling clear differentiation between intercalation-assisted and confinement-driven storage pathways. *Ex situ* Raman spectroscopy confirms the occurrence of intercalation in all three systems. At the same time, *ex situ* EPR analyses verify the presence of pseudo-metallic species at 0 V for Li and Na cells. Furthermore, density functional theory calculations elucidate the influence of interlayer spacing and micropore size on alkali-ion binding energetics. This highlights that Na ions benefit most from combining large interlayer spacing and accessible micropores, explaining their superior electrochemical performance. Overall, this work provides mechanistic insights into alkali-ion storage in closed-pore hard carbons and offers design guidelines for developing sustainable, high-performance, and broadly applicable anode materials for next-generation alkali-ion batteries. The combined experimental–computational approach presented here, systematically comparing Li-, Na-, and K-ion storage within the same carbon architecture, establishes a unified framework for understanding and optimizing alkali-ion storage mechanisms.

Author contributions

Nagmani: conceptualization, methodology, investigation, visualization, formal analysis, software, TOC, and writing – original draft, review & editing. Deepak Kumar Gorai: simulations and resources. Priyanka Pal: methodology, TOC, and validation. Sanchita Manna: methodology. Raju Kumar Gupta: funding acquisition and resources. Sreeraj Puravankara: conceptualization, supervision, visualization, resources, writing – review & editing, funding acquisition, and project administration.

Conflicts of interest

There are no conflicts of interest to declare.

Data availability

Should any raw data files be required, they are available from the corresponding author upon reasonable request. The authors confirm that the data supporting the findings of this study are available within the article [and/or] its supplementary information (SI). Supplementary information: experimental section, XRD, TEM, SAXS, cycling performance, *operando* XRD, CV, EIS, DFT analysis, *etc.* See DOI: https://doi.org/10.1039/d5ta10571d.

Acknowledgements

This work received funding from the Tata Chemicals Society for Rural Development (TCSRD) (grant no. PONIB001) and Science and Engineering Research Board (SERB), India (grant no. IPA/2021/000031). Nagmani acknowledges IIT Kharagpur for providing the central research facilities for specific measurements. The authors also sincerely thank Dr Brajesh (IIT Kanpur) for his kind assistance in carrying out the *operando* XRD measurements and analysis.

Notes and references

1 Y. Yang, Z. Liu, Q. Zhang, J. Song, W. Li, S. Jiang, C. Zhang, J. Han, H. Yang, X. Han and S. He, *Adv. Funct. Mater.*, 2025, 1–51.

2 J. Cui, P. Su, W. Li, X. Wang, Y. Zhang, Z. Xiao, Q. An and Z. Chen, *Adv. Energy Mater.*, 2025, **15**(16), 1–22.

3 Nagmani, P. Verma and S. Puravankara, *Langmuir*, 2022, **38**(50), 15703–15713.

4 L. Wang, Z. Xu, P. Lin, Y. Zhong, X. Wang, Y. Yuan and J. Tu, *Adv. Energy Mater.*, 2025, **15**(7), 1–10.

5 M. Ishaq, M. Jabeen, Y. S. He, H. Che, W. Xu, S. Zhao, Y. Shen, L. Li and Z. F. Ma, *Adv. Energy Mater.*, 2025, **15**(16), 1–14.

6 B. Xiao, T. Rojo and X. Li, *ChemSusChem*, 2019, **12**(1), 133–144.

7 H. Hou, X. Qiu, W. Wei, Y. Zhang and X. Ji, *Adv. Energy Mater.*, 2017, **7**(24), 201602898.

8 H. He, D. Sun, Y. Tang, H. Wang and M. Shao, *Energy Storage Materials*, 2019, **23**, 233–251.

9 Nagmani, D. Pahari, P. Verma and S. Puravankara, *J. Energy Storage*, 2022, **56**, 105961.

10 Y. Zhu, M. Chen, Q. Li, C. Yuan and C. Wang, *Carbon*, 2017, **123**, 727–734.

11 A. Beda, C. Vaulot, F. Rabuel, M. Morcrette and C. Matei Ghimbeu, *Energy Adv.*, 2022, **1**(4), 185–190.

12 Nagmani, A. Tyagi and S. Puravankara, *Mater. Adv.*, 2022, **3**(2), 810–836.

13 R. Alcántara, P. Lavela, G. F. Ortiz and J. L. Tirado, *Electrochem. Solid-State Lett.*, 2005, **8**(4), 225–228.

14 L. Shen, S. Shi, S. Roy, X. Yin, W. Liu and Y. Zhao, *Adv. Funct. Mater.*, 2021, **31**(4), 2006066.

15 Nagmani, A. Kumar and S. Puravankara, *Battery Energy*, 2022, **1**(3), 20220007.

16 S. Komaba, W. Murata, T. Ishikawa, N. Yabuuchi, T. Ozeki, T. Nakayama, A. Ogata, K. Gotoh and K. Fujiwara, *Adv. Funct. Mater.*, 2011, **21**(20), 3859–3867.

17 K. Kubota and S. Komaba, Review—Practical Issues and Future Perspective for Na-Ion Batteries, *J. Electrochem. Soc.*, 2015, **162**(14), A2538–A2550.

18 E. Irisarri, A. Ponrouch and M. R. Palacin, *J. Electrochem. Soc.*, 2015, **162**(14), A2476–A2482.

19 (*a*) C. Xiaoyang, S. Nurbiye, C. Kean, L. Hui, Z. Jun, W. Zhe, Y. Mei, T. Guo and C. Yuliang, *Energy Environ. Sci.*, 2023, **16**, 4041–4053; (*b*) M. Wahid, D. Puthusseri, Y. Gawli, N. Sharma and S. Ogale, *ChemSusChem*, 2018, **11**(3), 506–526.

20 K. Kubota, S. Shimadzu, N. Yabuuchi, S. Tominaka, S. Shiraishi, M. Abreu-Sepulveda, A. Manivannan, K. Gotoh, M. Fukunishi, M. Dahbi and S. Komaba, *Chem. Mater.*, 2020, **32**(7), 2961–2977.

21 Y. Huang, Y. Wang, P. Bai and Y. Xu, *ACS Appl. Mater. Interfaces*, 2021, **13**(32), 38441–38449.

22 H. Au, H. Alptekin, A. C. S. Jensen, E. Olsson, C. A. O'Keefe, T. Smith, M. Crespo-Ribadeneyra, T. F. Headen, C. P. Grey, Q. Cai, A. J. Drew and M. M. Titirici, *Energy Environ. Sci.*, 2020, **13**(10), 3469–3479.

23 S. Qiu, L. Xiao, M. L. Sushko, K. S. Han, Y. Shao, M. Yan, X. Liang, L. Mai, J. Feng, Y. Cao, X. Ai, H. Yang and J. Liu, *Adv. Energy Mater.*, 2017, **7**(17), 1700403.

24 Nagmani and S. Puravankara, *ACS Appl. Energy Mater.*, 2020, **3**(10), 10045–10052.

25 L. F. Zhao, Z. Hu, W. H. Lai, Y. Tao, J. Peng, Z. C. Miao, Y. X. Wang, S. L. Chou, H. K. Liu and S. X. Dou, *Adv. Energy Mater.*, 2021, **11**, 2002704.

26 (*a*) L. Liu, L. Gu, B. Shahid, K. Ramesh, F. Yongjin and C. Yuliang, *Adv. Energy Mater.*, 2026, **16**(4), e04853; (*b*) K. Wang, Y. Xu, H. Wu, R. Yuan, M. Zong, Y. Li, V. Dravid, W. Ai and J. Wu, *Carbon*, 2021, **178**, 443–450.

27 H. Moriwake, A. Kuwabara, C. A. J. Fisher and Y. Ikuhara, *RSC Adv.*, 2017, **7**(58), 36550–36554.

28 A. Vasileiadis, Y. Li, Y. Lu, Y. S. Hu and M. Wagemaker, *ACS Appl. Energy Mater.*, 2023, **6**(1), 127–140.

29 Nagmani, A. Kumar, C. Gowthami, R. Vijay, T. Narasinga Rao and S. Anandan, *Energy Fuels*, 2024, **38**(19), 18153–18168.

30 T. E. Rosser, E. J. F. Dickinson, R. Raccichini, K. Hunter, A. D. Searle, C. M. Kavanagh, P. J. Curran, G. Hinds, J. Park and A. J. Wain, *J. Electrochem. Soc.*, 2021, **168**(7), 070541.

31 X. Yin, Z. Lu, J. Wang, X. Feng, S. Roy, X. Liu, Y. Yang, Y. Zhao and J. Zhang, *Adv. Mater.*, 2022, **34**, 2109282.

32 J. S. Weaving, A. Lim, J. Millichamp, T. P. Neville, D. Ledwoch, E. Kendrick, P. F. McMillan, P. R. Shearing, C. A. Howard and D. J. L. Brett, *ACS Appl. Energy Mater.*, 2020, **3**(8), 7474–7484.

33 F. Geng, Q. Yang, C. Li, B. Hu, C. Zhao, M. Shen and B. Hu, *J. Phys. Chem. Lett.*, 2021, **12**(2), 781–786.

34 Nagmani, S. Manna and S. Puravankara, *Chem. Commun.*, 2024, **60**(22), 3071–3074.

35 C. Heubner, K. Nikolowski, S. Reuber, M. Schneider, M. Wolter and A. Michaelis, *Batteries Supercaps*, 2021, **4**(2), 268–285.

36 D. Wu, J. He, J. Liu, M. Wu, S. Qi, H. Wang, J. Huang, F. Li, D. Tang and J. Ma, *Adv. Energy Mater.*, 2022, **12**(18), 2200337.

37 H. Du, Y. Wang, Y. Kang, Y. Zhao, Y. Tian, X. Wang, Y. Tan, Z. Liang, J. Wozny, T. Li, D. Ren, L. Wang and X. He, *Adv. Mater.*, 2024, **36**(29), 2401482.

38 Y. Jiang and J. Liu, *Energy Environ. Mater.*, 2019, **2**(1), 30–37.

39 Z. Jian, Z. Xing, C. Bommier, Z. Li and X. Ji, *Adv. Energy Mater.*, 2016, **6**(3), 1501874.

40 Z. E. Yu, Y. Lyu, Y. Wang, S. Xu, H. Cheng, X. Mu, J. Chu, R. Chen, Y. Liu and B. Guo, *Chem. Commun.*, 2020, **56**(5), 778–781.

41 L. Zhuang, J. Lu, X. Ai and H. Yang, *J. Electroanal. Chem.*, 1995, 315–319.

42 L. Caracciolo, L. Madec and H. Martinez, *ACS Appl. Energy Mater.*, 2021, **4**(10), 11693–11699.

43 P. Hao, T. Zhu, Q. Su, J. Lin, R. Cui, X. Cao, Y. Wang and A. Pan, *Front. Chem.*, 2018, **6**, 1–9.

44 C. Sole, N. E. Drewett and L. J. Hardwick, *Faraday Discuss.*, 2014, **172**, 223–237.

45 L. J. Hardwick, H. Buqa and P. Novák, *Solid State Ionics*, 2006, **177**, 2801–2806.

46 M. A. Pimenta, G. Dresselhaus, M. S. Dresselhaus, L. G. Cançado, A. Jorioa and R. Saitoe, *Phys. Chem. Chem. Phys.*, 2007, **9**, 1276–1290.

47 X. Chen, J. Tian, P. Li, Y. Fang, Y. Fang, X. Liang, J. Feng, J. Dong, X. Ai, H. Yang and Y. Cao, *Adv. Energy Mater.*, 2022, **12**(24), 1–13.

48 Y. Cao, L. Xiao, M. L. Sushko, W. Wang, B. Schwenzer, J. Xiao, Z. Nie, L. V. Saraf, Z. Yang and J. Liu, *Nano Lett.*, 2012, **12**(7), 3783–3787.

49 E. Olsson, J. Cottom, H. Au, Z. Guo, A. C. S. Jensen, H. Alptekin, A. J. Drew, M. M. Titirici and Q. Cai, *Adv. Funct. Mater.*, 2020, **30**(17), 201908209.

50 H. Sun, Q. Zhang, Y. Ma, Z. Li, D. Zhang, Q. Sun, Q. Wang, D. Liu and B. Wang, *Energy Storage Mater.*, 2024, **67**, 103269.

51 K. Schutjajew, T. Tichter, J. Schneider, M. Antonietti, C. Roth and M. Oschatz, *Phys. Chem. Chem. Phys.*, 2021, **23**(19), 11488–11500.